International Journal of Multiphase Flow 35 (2009) 747–759

Contents lists available at ScienceDirect

International Journal of Multiphase Flow

journal homepage: www.elsevier.com/locate/ijmulflow

# Diffuse interface model for high speed cavitating underwater systems

Fabien Petitpas [a,*], Jacques Massoni [a], Richard Saurel [a,b], Emmanuel Lapebie [c], Laurent Munier [c]

[a] SMASH Group, Aix-Marseille Université UMR CNRS 6595, IUSTI–INRIA, 5 rue E. Fermi, 13453 Marseille Cedex 13, France
[b] University Institute of France, 5 rue E. Fermi, 13453 Marseille Cedex 13, France
[c] DGA, Centre d'Etudes de Gramat, 46500 Gramat, France

ARTICLE INFO

*Article history:*
Received 16 June 2008
Received in revised form 23 March 2009
Accepted 23 March 2009
Available online 22 April 2009

ABSTRACT

High speed underwater systems involve many modelling and simulation difficulties related to shocks, expansion waves and evaporation fronts. Modern propulsion systems like underwater missiles also involve extra difficulties related to non-condensable high speed gas flows. Such flows involve many continuous and discontinuous waves or fronts and the difficulty is to model and compute correctly jump conditions across them, particularly in unsteady regime and in multi-dimensions. To this end a new theory has been built that considers the various transformation fronts as 'diffuse interfaces'. Inside these diffuse interfaces relaxation effects are solved in order to reproduce the correct jump conditions. For example, an interface separating a compressible non-condensable gas and compressible water is solved as a multiphase mixture where stiff mechanical relaxation effects are solved in order to match the jump conditions of equal pressure and equal normal velocities. When an interface separates a metastable liquid and its vapor, the situation becomes more complex as jump conditions involve pressure, velocity, temperature and entropy jumps. However, the same type of multiphase mixture can be considered in the diffuse interface and stiff velocity, pressure, temperature and Gibbs free energy relaxation are used to reproduce the dynamics of such fronts and corresponding jump conditions. A general model, based on multiphase flow theory is thus built. It involves mixture energy and mixture momentum equations together with mass and volume fraction equations for each phase or constituent. For example, in high velocity flows around underwater missiles, three phases (or constituents) have to be considered: liquid, vapor and propulsion gas products. It results in a flow model with 8 partial differential equations. The model is strictly hyperbolic and involves waves speeds that vary under the degree of metastability. When none of the phase is metastable, the non-monotonic sound speed is recovered. When phase transition occurs, the sound speed decreases and phase transition fronts become expansion waves of the equilibrium system. The model is built on the basis of asymptotic analysis of a hyperbolic total non-equilibrium multiphase flow model, in the limit of stiff mechanical relaxation. Closure relations regarding heat and mass transfer are built under the examination of entropy production. The mixture equation of state (EOS) is based on energy conservation and mechanical equilibrium of the mixture. Pure phases EOS are used in the mixture EOS instead of cubic one in order to prevent loss of hyperbolicity in the spinodal zone of the phase diagram. The corresponding model is able to deal with metastable states without using Van der Waals representation.

The model's predictions are validated in multi-dimensions against experiments of high velocity projectile impact onto a liquid tank. Simulations are compared to experiments and reveal excellent quantitative agreement regarding shock and cavitation pocket dynamics as well as projectile deceleration versus time. Then model's capabilities are illustrated for flow computations around underwater missiles.



## 1. Introduction

The numerical simulation of modern underwater propulsion system involves many scientific challenges. Among them, material interfaces are present due to the combustion gas products injected through the nozzle into water from the solid rocket motor. As the underwater system is moving at high velocity, zones at low pressure appear in the wake of the missile and at geometrical singularities. In these zones, liquid water may reach a metastable state where the temperature is higher than the saturated one at the local pressure. Thus evaporation fronts appear transforming liquid water to vapor or liquid–vapor mixture. The typical problem under interest is schematized in Fig. 1 where an underwater missile is moving at high velocity.

From a modelling point of view, the flow model has to account for:

* Corresponding author. Tel.: +33 4 91 10 69 34; fax: +33 4 91 10 69 69.
*E-mail addresses:* Fabien.Petitpas@polytech.univ-mrs.fr (F. Petitpas), Richard.Saurel@polytech.univ-mrs.fr (R. Saurel).

0301-9322/$ - see front matter © 2009 Elsevier Ltd. All rights reserved.
doi:10.1016/j.ijmultiphaseflow.2009.03.011

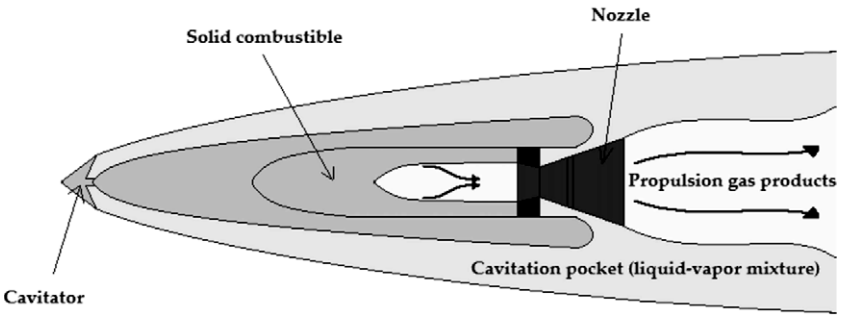


**Fig. 1.** Underwater missile moving at high velocity. Natural cavitation pockets appear at locations where geometrical effects produce metastable liquid state. Combustion gases injected through the rocket nozzle interact with surrounding liquid and vapor.

- Liquid and gas compressiblity and associated waves dynamics (shocks, expansion waves and contact discontinuities).
- Material interfaces of simple contact, where normal velocity and pressure must be continuous.
- Evaporating interfaces that appear dynamically at locations where the liquid is metastable, forming cavitation pockets.

In the authors knowledge, such effects have never been accounted simultaneously in a simulation work. The last point, associated to cavitation pockets is often considered as isentropic (Liu et al., 2004). In this frame, cavitation pockets result of mechanical bubble growth only. In the present work, cavitation pockets result of both mass transfer and mechanical bubble growth.

The presence of such a variety of waves, discontinuities and fronts renders impracticable numerical strategies based on sharp discontinuities representation, like front tracking or interface reconstruction. It is the reason that yields us to the development of a diffuse interface theory, on the basis of multiphase flow modeling. In this approach, each discontinuity is solved as a diffuse zone, like shock capturing methods deal with shock waves in gas dynamics. The difficulty with these methods is to determine the correct formulation and the appropriate numerics in order to match jump conditions. This is the research direction adopted by the Smash Group 15 years ago.

In Saurel and Abgrall (1999) a multiphase flow model with seven equations, involving two pressures, two velocities and two temperatures was used to solve interface problems of simple contact in order to match equal normal velocities and pressures jump conditions. This method shown its efficiency for any material flowing in hydrodynamic regime (gas, liquid or solid) separated by interfaces. The key point was the use of infinitely fast relaxation parameters in the interfacial diffuse zone in order to relax the two pressures and two velocity toward their equilibrium values. The same strategy could be used for the present application, as liquid–gas interfaces are present, except that phase transition appears naturally.

More recently (Saurel et al., 2008) phase transition has been implemented in the diffuse interface formulation in the context of two-phases only. The corresponding model was able to deal, as limit cases, with interfaces of simple contact (i.e. without phase transition) and with evaporating/condensating interfaces. This model also uses a two-phase formulation, but the stiff mechanical relaxation responsible for the fulfillment of simple contact interface conditions is inherent to the model. Indeed, the multiphase model involves a single pressure and a single velocity (Kapila et al., 2001), and is able under proper numerical resolution to solve interface problems very efficiently (Saurel et al., 2009). With the special relaxation procedure developed in (Saurel et al., 2008) the model is able to deal with evaporation fronts propagating in metastable liquids. It has been validated against basic experiments of evaporation waves in expansion tubes (Simoes-Moreira and Shepherd, 1999).

However, an important development of the model is necessary to deal with the present application. The model has to deal with both condensable and non-condensable gases. This yields an important difference regarding interface conditions. With condensable gases and evaporating liquids, the interface condition involves velocity and pressure jumps while with non-condensable gases these variables have to be continuous. To deal with such situation, the flow model of Saurel et al. (2008) is extended to an arbitrary number of phases or constituents. The relaxation method used to match interface conditions with evaporating interfaces is used when necessary i.e. when evaporation between two fluids is possible and when local thermodynamic conditions correspond to metastability for a given phase. The generalization of the model and method to an arbitrary number of fluids, condensable and non-condensable is the main goal of the present paper. It is indeed the key point to solve flows with various types of interfaces.

The paper is organized as follows. The flow model with an arbitrary number of constituents is derived in Section 2. A multiphase model to solve interfaces of simple contact with heat transfer but without mass transfer is presented as a reduction of a total non-equilibrium model of Baer and Nunziato (1986) type. This model has the ability to solve interface problems between non-miscible fluids. Then mass transfer effects are added to the model. Corresponding relaxation terms are built on the basis of the entropy production of the system. The corresponding model is able to deal with evaporation fronts, flashing and cavitation. The thermodynamic closure is summarized in Section 3. Each phase possesses its own EOS and the mixture obeys to a mixture EOS able to reproduce the non-monotonic (Wood, 1930) speed of sound as well as another non-monotonic (but lower) sound speed when mass transfer is present. Numerical results are presented in Section 4. The model is first validated on problems with interfaces separating non-miscible fluids for which exact solutions are available. Then, results with mass transfer are considered, first in one dimension then in two dimensions. The impact of a high velocity projectile onto a liquid tank is examined. Computed shock dynamics into water and cavitation pocket in the wake of the projectile are compared to experimental measurements. The projectile deceleration versus time is also recorded and compared to the experiments. All comparisons show excellent agreement. Last, the flow around an underwater missile is computed to illustrate model's capabilities.

## 2. Derivation of the model

The flow model we are seeking has to deal with interfaces of simple contact and evaporating interfaces under a unique mathematical formulation. As wave dynamics is under interest the governing equations must form a hyperbolic system. A formulation involving an arbitrary number of constituents (or phases) out of

thermal equilibrium is also mandatory in order to consider the appropriate thermodynamics of each constituent: combustion gases, liquid and its vapor. The multiphase mixture of these constituents will be treated as a homokinetic mixture with a unique pressure but several temperatures. Phase transition has to be considered across evaporating interfaces and in the mixture. In order to circumvent ill-posedness issues associated to cubic EOS (van der Waals for example) the relaxation method of (Saurel et al., 2008) will be extended to the present context involving an arbitrary number of phases.

The derivation of the flow model follows the lines of Saurel et al. (2008) where a two-phase mixture only was considered. The main steps of this method can be summarized as:

(i) The starting point of the modelling is a two phase model in total disequilibrium. It involves two velocities, two pressures and two temperatures. Heat exchange is considered but mass transfer is omitted. Indeed, mass transfer modeling in a two-velocities approach is an issue, particularly when each phase is compressible.
(ii) With the help of asymptotic expansions in the limit of stiff mechanical relaxation this model is reduced to a single velocity and single pressure model, including heat exchanges (Kapila et al., 2001). This model is able to deal with diffuse interfaces (Murrone and Guillard, 2005; Petitpas et al., 2007; Saurel et al., 2009). It is important to note that temperature relaxation is not considered in the same limit. Thus the developed model is a diffuse interface model with one velocity, one pressure but two temperatures.
(iii) Then, mass transfer effects are considered in the single velocity reduced model. It consists in modifying mass and volume fraction equations in order to take into account the changes related to this physical effect. The forms of added terms have to be determined in order to close the model.
(iv) The phase's entropy equations are determined and analysed allowing the determination of the volume fraction rate of change due to mass transfer.
(v) The last step is based on the second law of thermodynamics applied to the mixture. Entropy production yields the well-posed form of the mass transfer terms allowing closure of the system. The kinetic parameters involved in these relaxation terms can be considered as zero at simple contact interface while they are considered infinite at evaporation fronts (Saurel et al., 2008). Consequently evaporation fronts are considered at thermodynamic equilibrium.

This derivation method, proposed in Saurel et al. (2008), is the same as the one used in the following section to develop the multiphase extension of the model. Nevertheless, difficulties have to be solved for some points. The details are given when necessary.

### 2.1. Step (i): the total non-equilibrium 'parent' model

The construction of the multiphase single pressure and single velocity model we are seeking is based on the asymptotic reduction of the following Baer and Nunziato (1986) type non-equilibrium multiphase model. The system is composed with four equations for each phase:

$$\begin{cases} \frac{\partial \alpha_k}{\partial t} + \vec{u}_I \cdot \vec{\nabla}\alpha_k = \alpha_k \mu (p_k - p_*), \\ \frac{\partial \alpha_k \rho_k}{\partial t} + div(\alpha_k \rho_k \vec{u}_k) = 0, \\ \frac{\partial \alpha_k \rho_k \vec{u}_k}{\partial t} + div(\alpha_k \rho_k \vec{u}_k \otimes \vec{u}_k) + \vec{\nabla}(\alpha_k p_k) = p_I \vec{\nabla}\alpha_k + Y_k \lambda (\vec{u}_* - \vec{u}_k) \\ \frac{\partial \alpha_k \rho_k E_k}{\partial t} + div(\alpha_k (\rho_k E_k + p_k)\vec{u}_k) = p_I \vec{u}_I \cdot \vec{\nabla}\alpha_k + Y_k \lambda \vec{u}_I \cdot (\vec{u}_* - \vec{u}_k) \\ \quad -\alpha_k p_I \mu (p_k - p_*) + Q_k \end{cases} \tag{1}$$

We denote, respectively, by $\alpha_k$, $\rho_k$, $\vec{u}_k$, $p_k$, $E_k$ and $e_k$ the volume fraction, the density, the velocity vector, the pressure, the total specific energy and the internal specific energy of the phase $k$. The total specific energy is defined by $E_k = e_k + \|\vec{u}_k\|^2/2$.

There are different possibilities to model heat transfer terms $Q_k$. A possible modeling is $Q_k = H_k(T_* - T_k)$ where $H_k = h \cdot S_{k,I}$ involves the convective heat transfer coefficient $h$ and the specific exchange surface $S_{k,I}$ of phase $k$. Mixture pressure, velocity and temperature are defined by:

$$p_* = \sum_k \alpha_k p_k,$$

$$\vec{u}_* = \sum_k Y_k \vec{u}_k,$$

$$T_* = \sum_k Y_k C v_k T_k \Big/ \sum_k Y_k C v_k.$$

where the mass fraction is defined by $Y_k = \alpha_k \rho_k / \rho$ and the mixture density is defined by $\rho = \sum_k \alpha_k \rho_k$.

Entropy equations can be written under the form:

$$\alpha_k \rho_k T_k \frac{ds_k}{dt} = (p_I - p_k)(\vec{u}_I - \vec{u}_k) \cdot \vec{\nabla}\alpha_k + Y_k \lambda (\vec{u}_* - \vec{u}_k)^2 - \alpha_k \mu (p_k - p_*)^2 + Q_k$$

Regarding positivity of the first term on the right-hand side, appropriate estimates for the interfacial pressure $p_I$ and velocity $\vec{u}_I$ are given in Saurel et al. (2003) or Chinnayya et al. (2004) where a symmetric formulation is developed. It is not necessary to detail these interfacial variables as we are seeking a mechanical equilibrium model where all phasic pressures and velocities are equal.

System (1) guarantees conservation for the mixture and is frame invariant. The interaction terms that appear in the right-hand side express the effects that drive the system to mechanical equilibrium by the way of relaxation coefficients $\mu$ and $\lambda$.

This system is unconditionally hyperbolic and admits the characteristic waves speeds: $u_k, u_k + c_k, u_k - c_k$ for each phase $k$ and the interface velocity $u_I$.

The thermodynamic closure of System (1) is achieved by appropriate convex EOS for each phase: $p_k = p_k(\rho_k, e_k)$. Here each phase is governed by its own EOS, corresponding to the one of the pure substance. Example of gas and condensed phase EOS is given in Section 3.

### 2.2. Step (ii): the diffuse interface flow model without mass transfer

When dealing with interfaces only, System (1) involves unnecessary effects (multi-velocities and multi-pressures) and a reduced model is preferred. We are seeking the simplest model involving the pertinent physics: interfaces solved as diffused multiphase mixtures zones. During this reduction step, non-equilibrium thermal effects are retained but mechanical equilibrium ones are relaxed. Mass transfer consideration will be addressed in further section. The reduced system able to deal with interfaces of simple contact is obtained in the limit of stiff mechanical relaxation:

$$\mu = \frac{1}{\epsilon}, \quad \lambda = \frac{1}{\epsilon} \qquad \text{where} \quad \epsilon \to 0^+.$$

The derivation is done in Saurel et al. (2008) in the context of two fluids. The model with an arbitrary number of phases is composed of two equations for each phase and two equations for the mixture:

$$\begin{cases} \frac{\partial \alpha_k}{\partial t} + \vec{u} \cdot \vec{\nabla}\alpha_k = \alpha_k \left( \frac{\rho c^2}{\rho_k c_k^2} - 1 \right) div(\vec{u}) + \left( \frac{Q_k \Gamma_k}{\rho_k c_k^2} - \alpha_k \frac{\rho c^2}{\rho_k c_k^2} \sum_j \frac{Q_j \Gamma_j}{\rho_j c_j^2} \right) \\ \frac{\partial \alpha_k \rho_k}{\partial t} + div(\alpha_k \rho_k \vec{u}) = 0 \\ \frac{\partial \rho \vec{u}}{\partial t} + div(\rho \vec{u} \otimes \vec{u}) + \vec{\nabla} p = 0 \\ \frac{\partial \rho E}{\partial t} + div((\rho E + p)\vec{u}) = 0 \end{cases} \tag{2}$$

Here, $c_k$ represents the speed of sound of phase $k$:

$$\forall k, \qquad c_k^2 = \frac{\frac{p}{\rho_k^2} - \left(\frac{\partial e_k}{\partial \rho_k}\right)_p}{\left(\frac{\partial e_k}{\partial p}\right)_{\rho_k}},$$

and $\Gamma_k$ represents the Gruneisen coefficient of phase $k$:

$$\forall k, \qquad \Gamma_k = v_k \left(\frac{\partial p}{\partial e_k}\right)_{\rho_k}$$

where $v_k = 1/\rho_k$.

The mixture total energy is defined by $E = \sum_k Y_k e_k + 1/2u^2$.

Entropy equations for this model read:

$$\forall k, \qquad \frac{ds_k}{dt} = \frac{Q_k}{\alpha_k \rho_k T_k}$$

With the same definition of heat exchanges as in System (1). There is no difficulty to show that entropy production for the mixture is positive. The thermodynamic closure of System (2) is achieved by the pressure equilibrium constraint: $p_k(\rho_k, e_k) = p'_k(\rho'_k, e'_k)$.

With the help of the phase's EOS and mixture energy definition, a mixture EOS can be derived, as will be done in Section 3. With this definition of the equilibrium pressure, the system admits the Wood (1930) non-monotonic speed of sound.

Under this form System (2) is able to deal with interfaces of simple contact, with or without heat transfer. It has been validated against exact solutions in one-dimension (Riemann problems) and has shown its ability for multi-dimensional computations (Murrone and Guillard, 2005; Petitpas et al., 2007; Saurel et al., 2009). The next step is to introduce mass transfer in the diffuse interface model in order to deal with phase transition and cavitation pocket appearance.

### 2.3. Step (iii): mass transfer modelling in the diffuse interface method

System (2) describes a compressible multi-phase mixture in mechanical equilibrium but out of thermal equilibrium. The introduction of mass transfer effects has been considered in Saurel et al. (2008) in the context of two phases only. Here the method is extended to an arbitrary number of phases. The addition of mass transfer modifies the mass equation of each fluid:

$$\forall k, \qquad \frac{\partial \alpha_k \rho_k}{\partial t} + div(\alpha_k \rho_k \vec{u}) = \rho \dot{Y}_k$$

where $\rho \dot{Y}_k$ represents the mass transfer of phase $k$. Expression for this mass transfer has to be determined. Mass transfer implies changes in the volume fraction. We assume that the volume fraction equation becomes:

$$\forall k, \quad \frac{\partial \alpha_k}{\partial t} + \vec{u} \cdot \vec{\nabla} \alpha_k = \alpha_k \left(\frac{\rho c^2}{\rho_k c_k^2} - 1\right) div(\vec{u}) + \left(\frac{Q_k \Gamma_k}{\rho_k c_k^2} - \alpha_k \frac{\rho c^2}{\rho_k c_k^2} \sum_j \frac{Q_j \Gamma_j}{\rho_j c_j^2}\right) + \dot{\alpha}_k \tag{3}$$

where the volume fraction source terms $\dot{\alpha}_k$ linked with mass transfer have to be determined too. The determination of the expressions for mass transfer terms $\dot{Y}_k$ and volume fraction source terms $\dot{\alpha}_k$ is based upon the analysis of the entropy production in each phase and for the system. The next step is thus to determine the entropy equation for each fluid.

### 2.4. Step (iv): determination of the entropy equations of the phases

The entropy equations are determined as solutions of an algebraic system built on the basis of:

- energy conservation of the mixture,
- pressure equilibrium between phases.

Let us first examine the constraint given by energy conservation to the entropy equations. By using the energy and momentum equations of System (2), a simpler form of the energy equation is obtained:

$$\frac{de}{dt} + p \frac{dv}{dt} = 0, \tag{4}$$

where the mixture internal energy is defined by $e = \sum_k Y_k e_k$ and the mixture specific volume is given by $v = \sum_k Y_k v_k$. Thus (4) becomes:

$$\sum_k Y_k \left(\frac{de_k}{dt} + p \frac{dv_k}{dt}\right) + \sum_k h_k \dot{Y}_k = 0.$$

Here $h_k = e_k + p v_k$ is the enthalpy of the phase $k$. By using Gibbs identity for each phase $k$, we have:

$$\forall k, \quad \frac{de_k}{dt} + p \frac{dv_k}{dt} = T_k \frac{ds_k}{dt}.$$

The mixture energy equation now becomes:

$$\sum_k Y_k T_k \frac{ds_k}{dt} + \sum_k h_k \dot{Y}_k = 0. \tag{5}$$

This last equation involves the $N$ functions $ds_k/dt$ that we have to determine. The $(N-1)$ other relations are obtained with the mechanical equilibrium condition:

$$\forall k, \ \forall k' \neq k, \quad p_k(\rho_k, s_k) = p_{k'}(\rho_{k'}, s_{k'}). \tag{6}$$

Upon differentiation along fluid trajectories, we get:

$$\forall k, \forall k' \neq k, \ \left(\frac{\partial p_k}{\partial \rho_k}\right)_{s_k} \frac{d\rho_k}{dt} + \left(\frac{\partial p_k}{\partial s_k}\right)_{\rho_k} \frac{ds_k}{dt} = \left(\frac{\partial p_{k'}}{\partial \rho_{k'}}\right)_{s_{k'}} \frac{d\rho_{k'}}{dt} + \left(\frac{\partial p_{k'}}{\partial s_{k'}}\right)_{\rho_{k'}} \frac{ds_{k'}}{dt}.$$

With the help of the sound's speed and Gruneisen coefficient for the phases,

$$\forall k, \quad \left(\frac{\partial p_k}{\partial \rho_k}\right)_{s_k} = c_k^2 \qquad \text{and} \qquad \left(\frac{\partial p_k}{\partial s_k}\right)_{\rho_k} = \rho_k \Gamma_k \, T_k,$$

the $(N-1)$ mechanical equilibrium relations become:

$$\forall k, \ \forall k' \neq k, \quad c_k^2 \frac{d\rho_k}{dt} + \rho_k \Gamma_k \, T_k \frac{ds_k}{dt} = c_{k'}^2 \frac{d\rho_{k'}}{dt} + \rho_{k'} \Gamma_{k'} \, T_{k'} \frac{ds_{k'}}{dt} \tag{7}$$

Eqs. (5) and (7) form a system of $N$ equations with the $N$ unknowns functions $ds_k/dt$. Resolution of this system yields:

$$\forall k, \quad \rho_k T_k \frac{\Gamma_k}{\Gamma} \frac{ds_k}{dt} + \sum_{k' \neq k} \frac{\alpha_{k'}}{\Gamma_{k'}} \left(c_k^2 \frac{d\rho_k}{dt} - c_{k'}^2 \frac{d\rho_{k'}}{dt}\right) + \sum_j h_j \rho \dot{Y}_j = 0 \tag{8}$$

The next step is to replace the variations $d\rho_k/dt$ by space variations and source terms. This is done with the help of mass and volume fraction equations:

$$\forall k, \quad \frac{d\rho_k}{dt} = -\frac{\rho c^2}{c_k^2} div(\vec{u}) - \left(\frac{Q_k \Gamma_k}{\rho_k c_k^2} - \frac{\rho c^2}{c_k^2} \sum_j \frac{Q_j \Gamma_j}{\rho_j c_j^2}\right) + \frac{\rho \dot{Y}_k - \rho_k \dot{\alpha}_k}{\alpha_k} \tag{9}$$

Thus entropy Eq. (8) become:

$$\forall k, \quad \rho Y_k \frac{ds_k}{dt} = \frac{Q_k}{T_k} - \frac{\alpha_k \Gamma}{\Gamma_k T_k} \sum_j h_j \rho \dot{Y}_j + \frac{\alpha_k \Gamma}{\Gamma_k T_k} \sum_{k' \neq k} \times \frac{\alpha_{k'}}{\Gamma_{k'}} \left(c_{k'}^2 \frac{\rho \dot{Y}_{k'} - \rho_{k'} \dot{\alpha}_{k'}}{\alpha_{k'}} - c_k^2 \frac{\rho \dot{Y}_k - \rho_k \dot{\alpha}_k}{\alpha_k}\right) \tag{10}$$

Entropy equation for each phase (10) is composed of three terms. Each of them expresses a physical phenomenon responsible for entropy production:

- The first one is related to heat exchange.
- The second one is associated to mass transfer.
- The last term is associated to the pressure relaxation process associated to mass transfer.

To schematize physical meaning of the last term consider a pressure perturbation appearing during mass transfer, as shown in Fig. 2. The system turns back to mechanical equilibrium with the help of acoustic waves emitted during evaporation. This is similar to acoustic waves emitted by flames during their propagation, that render the flow quasi-isobaric. These acoustic waves are isentropic. We thus consider that the pressure relaxation process present during mass transfer is isentropic. This corresponds to cancellation of the third term in (10). This assumption provides the $N$ following constraints:

$$\forall k, \quad \sum_{k' \neq k} \frac{\alpha_{k'}}{\Gamma_{k'}} \left( c_{k'}^2 \frac{\rho \dot{Y}_{k'} - \rho_{k'} \dot{\alpha}_{k'}}{\alpha_{k'}} - c_k^2 \frac{\rho \dot{Y}_k - \rho_k \dot{\alpha}_k}{\alpha_k} \right) = 0$$

After some manipulation they can be rewritten under the form:

$$\forall k, \quad c_k^2 \frac{\rho \dot{Y}_k - \rho_k \dot{\alpha}_k}{\alpha_k \Gamma} = \sum_j c_j^2 \frac{\rho \dot{Y}_j - \rho_j \dot{\alpha}_j}{\Gamma_j}$$

This implies $(N-1)$ new relations:

$$\forall k' \neq k, \quad c_{k'}^2 \frac{\rho \dot{Y}_{k'} - \rho_{k'} \dot{\alpha}_{k'}}{\alpha_{k'}} = c_k^2 \frac{\rho \dot{Y}_k - \rho_k \dot{\alpha}_k}{\alpha_k}$$

Or,

$$\forall k' \neq k, \quad \dot{\alpha}_{k'} = \frac{\alpha_{k'}}{\rho_{k'} c_{k'}^2} \left( \frac{\rho_k c_k^2 \dot{\alpha}_k}{\alpha_k} + \frac{\rho \dot{Y}_{k'} c_{k'}^2}{\alpha_{k'}} - \frac{\rho \dot{Y}_k c_k^2}{\alpha_k} \right)$$

Using the saturation constraint the volume fractions rate of change due to mass transfer reads:

$$\forall k, \quad \dot{\alpha}_k = \frac{\rho \dot{Y}_k}{\rho_k} - \frac{\alpha_k}{\rho_k c_k^2} \rho c^2 \sum_j \frac{\rho \dot{Y}_j}{\rho_j} \tag{11}$$

This relation provides closure of the volume fraction equations we were seeking.

### 2.5. Step (v): mixture entropy inequality

The second principle of thermodynamics applied to the mixture reads:

$$\frac{\partial \rho s}{\partial t} + div(\rho s \vec{u}) \geqslant 0,$$

where the mixture entropy is defined by $s = \sum_k Y_k s_k$. With the assumption used to determine the rate of change of volume fractions (isentropic pressure relaxation process during mass transfer), Eq. (10) become:

$$\forall k, \quad \rho Y_k \frac{ds_k}{dt} = \frac{Q_k}{T_k} - \frac{\alpha_k \Gamma}{\Gamma_k T_k} \sum_j h_j \rho \dot{Y}_j \tag{12}$$

Using these expressions and mass equations in the entropy inequality leads to:

$$\sum_k \frac{Q_k}{T_k} - \sum_k \frac{\alpha_k \Gamma}{\Gamma_k T_k} \sum_j h_j \rho \dot{Y}_j + \sum_k s_k \rho \dot{Y}_k \geqslant 0$$

which can be reorganized as follows:

$$\sum_k \frac{Q_k}{T_k} - \frac{1}{T_I} \sum_k \bar{g}_k \rho \dot{Y}_k \geqslant 0 \tag{13}$$

where an "interface temperature" appears:

$$\frac{1}{T_I} = \Gamma \sum_k \frac{\alpha_k}{\Gamma_k T_k}$$

The extended Gibbs free energies also appear:

$$\forall k, \quad \bar{g}_k = h_k - T_I s_k$$

Positivity entropy production in (13) will be guaranteed with the following modeling of heat and mass transfer terms:

$$\forall k, \quad Q_k = \sum_{k' \neq k} H_{kk'} (T_{k'} - T_k),$$

$$\forall k, \quad \dot{Y}_k = \sum_{k' \neq k} v_{kk'} (\bar{g}_{k'} - \bar{g}_k)$$

where $H_{kk'}$ and $v_{kk'}$ are positive relaxation parameters that control the rate at which phases $k$ and $k'$ relax toward thermodynamic equilibrium. This corresponds to the form of mass transfer terms we were seeking. Note that this modelling of relaxation terms guarantees equilibrium conditions of equal temperatures and equal Gibbs free energies.

### 2.6. The diffuse interface model with heat and mass transfer

We now have a symmetric hyperbolic non-equilibrium compressible multi-phase flow mixture model with heat and mass exchanges

$$\begin{cases} \frac{\partial \alpha_k}{\partial t} + \vec{u} \cdot \vec{\nabla} \alpha_k = \alpha_k \left( \frac{\rho c^2}{\rho_k c_k^2} - 1 \right) div(\vec{u}) + \left( \frac{Q_k \Gamma_k}{\rho_k c_k^2} - \alpha_k \frac{\rho c^2}{\rho_k c_k^2} \sum_j \frac{Q_j \Gamma_j}{\rho_j c_j^2} \right) \\ \qquad + \frac{\rho \dot{Y}_k}{\rho_k} - \alpha_k \frac{\rho c^2}{\rho_k c_k^2} \sum_j \frac{\rho \dot{Y}_j}{\rho_j} \\ \frac{\partial \alpha_k \rho_k}{\partial t} + div(\alpha_k \rho_k \vec{u}) = \rho \dot{Y}_k \\ \frac{\partial \rho \vec{u}}{\partial t} + div(\rho \vec{u} \otimes \vec{u}) + \vec{\nabla} p = 0 \\ \frac{\partial \rho E}{\partial t} + div((\rho E + p) \vec{u}) = 0 \end{cases} \tag{14}$$

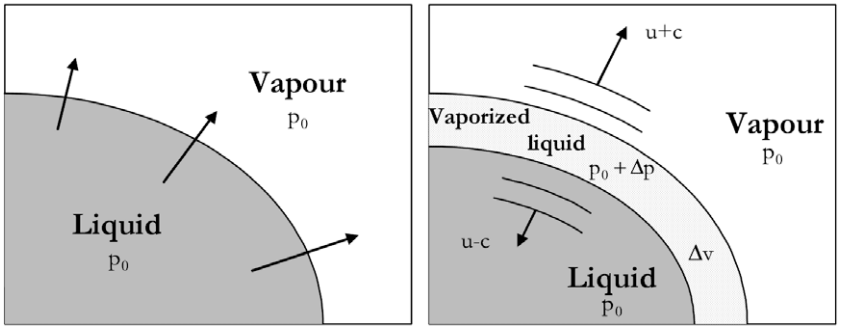


**Fig. 2.** Schematic representation of liquid evaporation. An elementary volume $\Delta v$ of liquid is transformed to vapor with a pressure perturbation. Acoustic waves propagates through liquid and vapor, reflect at volume boundaries and restore pressure equilibrium. The overall process is isentropic as these waves are of small amplitude. These waves are necessarily weak as evaporation is a continuous phenomenon. Elementary volume and pressure perturbations tend to zero.

where:

$$\forall k, \quad Q_k = \sum_{k' \neq k} H_{kk'}(T_{k'} - T_k)$$
$$\forall k, \quad \dot{Y}_k = \sum_{k' \neq k} v_{kk'}(\bar{g}_{k'} - \bar{g}_k)$$

The thermodynamic closure of System (14) is achieved by the pressure equilibrium constraint: $p_k(\rho_k, e_k) = p'_k(\rho'_k, e'_k)$. This condition will be transformed to a mixture EOS in Section 3.

The mixture entropy equation for System (14) reads:

$$\frac{\partial \rho s}{\partial t} + div(\rho s \vec{u}) = \sum_k \frac{Q_k}{T_k} - \frac{1}{T_I} \sum_k \bar{g}_k \rho \dot{Y}_k \geqslant 0$$

The determination of the temperature relaxation parameters $H_{kk'}$ for a multi-phase mixture with arbitrary interfacial area is a difficult issue. The same remark holds for the phase transition kinetics parameters $v_{kk'}$ that does not depend only of interfacial area but also of local chemical relaxation. To circumvent these difficulties, we use a solution procedure based on infinite relaxation parameters, but at selected spatial locations only. More precisely, in order to retain metastable states, the relaxation parameters $H_{kk'}$ and $v_{kk'}$ will be set to zero for locations far from liquid–vapor interfaces. When an interface separates a liquid and its vapor under metastable thermodynamic conditions, they will be taken infinite in order to fulfill equilibrium interface conditions with mass transfer. When dealing with interfaces of simple contact between a liquid and a non-condensable gas, they will be set to zero. Such procedure is summarized by:

$$H_{kk'}, v_{kk'} = \begin{cases} +\infty \text{ if } kk' \text{ represent a liquid—vapor pair with one of these two fluids} \\ \quad \text{in metastable state and } \epsilon \leqslant (\alpha_k, \alpha_{k'}) \leqslant 1 - \epsilon \\ 0 \text{ otherwise} \end{cases}$$

## 3. Thermodynamic closure

In most phase transition models a cubic equation of state (EOS) is used. Such EOS expresses the behavior of a fluid from pure liquid to pure vapor. These models present an incorrect feature regarding the square speed of sound that becomes negative in the spinodal zone of the two-phase region. It results in a loss of hyperbolicity in this domain, or in other words to incorrect wave dynamics and even computational failure. In order to circumvent this difficulty, the present model uses pure substance EOS for each fluid. It means that each phase will possess its own EOS. When a liquid and its vapor are under consideration, the various constants in these EOS are linked to each other in order to fulfill some constraints related to the phase diagram. In the present paper, we consider "stiffened gas" (SG) equations of state, but the method can be generalized to more complex convex equations of state.

The SG EOS or its generalized forms (Mie–Gruneisen (MG) EOS) are usually used for shock dynamics in condensed materials. The parameters used in these EOS are determined by using a reference curve, usually in the $(p, v)$ plane. In shock physics, the Hugoniot curve is used. A discussion about MG and SG EOS is given in Menikoff and Plohr (1989). It is also possible to use another reference curve to determine EOS parameters. In Le Metayer et al. (2004) saturation curves are used to determine SG parameters for liquid and vapor phases. These reference curves are indeed more relevant for phase transition.

Doing so, each fluid has its own thermodynamics and in particular its own entropy. In the present modelling of mass transfer, relaxation towards equilibrium is achieved by a kinetic process, contrarily to van der Waals modelling where mass transfer is a thermodynamic path (Fig. 3). It is the reason why the present modelling preserves hyperbolicity during mass transfer.

When equilibrium is reached, conventional properties of the phase diagram have to be recovered (latent heat of vaporization, saturation temperature) that depend on pressure or temperature. In other words, the two pure fluids EOS must be connected by some constraints. These constraints are used for the determination of the various constants involved in these EOSs.

For each phase the thermodynamic state is determined by the SG EOS that reads:

$$e(p, v) = \frac{p + \gamma p_\infty}{(\gamma - 1)} v + q \tag{15}$$
$$v(p, T) = \frac{(\gamma - 1) C_v T}{p + p_\infty} \tag{16}$$
$$h(T) = \gamma C_v T + q \tag{17}$$
$$g(p, T) = (\gamma C_v - q')T - C_v T \log \frac{T^\gamma}{(p + p_\infty)^{(\gamma - 1)}} + q \tag{18}$$

where $e, v = 1/\rho, p, T, h$ and $g$ are, respectively, the internal energy, the specific volume, the pressure, the temperature, the enthalpy and the Gibbs free energy of the considered phase. The constants, characteristic of each fluid are: $\gamma, p_\infty, C_v, q$ and $q'$. A method to determine these parameters in gas–liquid systems is given in Le Metayer et al. (2004). For liquid water and steam, corresponding parameters are summarized in Table 1. Liquid dodecane and steam SG EOS parameters are given in Table 2.

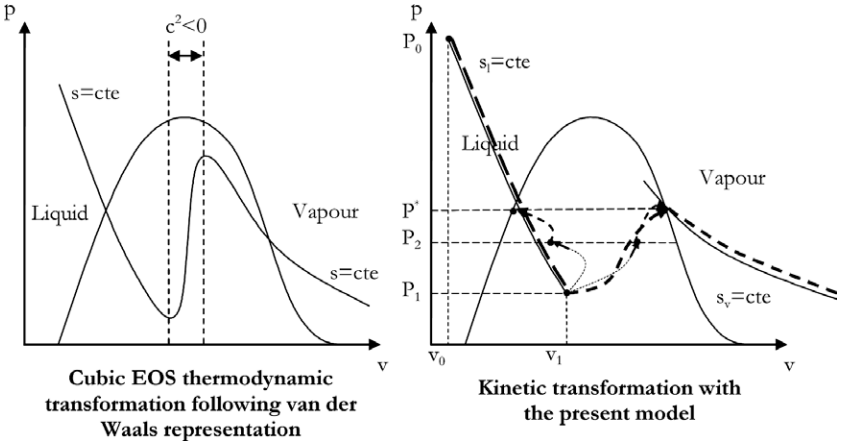


**Fig. 3.** Schematic representation of the thermodynamic path using a cubic EOS compared to the kinetic process represented in dashed line.

**Table 1**
Stiffened gas EOS parameters for liquid and vapor water.

| | $p_\infty$ (Pa) | $C_p$ (J/kg K) | $C_v$ (J/kg K) | $\gamma$ | $q$ (J/kg) | $q'$ (J/kg K) |
|---|---|---|---|---|---|---|
| Liquid | $10^9$ | 4267 | 1816 | 2.35 | $-1167 \times 10^3$ | 0 |
| Vapor | 0 | 1487 | 1040 | 1.43 | $2030 \times 10^3$ | $-23 \times 10^3$ |

**Table 2**
Stiffened gas EOS parameters for liquid and vapor dodecane.

| | $p_\infty$ (Pa) | $C_p$ (J/kg K) | $C_v$ (J/kg K) | $\gamma$ | $q$ (J/kg) | $q'$ (J/kg K) |
|---|---|---|---|---|---|---|
| Liquid | $4 \times 10^8$ | 2534 | 1077 | 2.35 | $-775 \times 10^3$ | 0 |
| Vapor | 0 | 2005 | 1956 | 1.025 | $-237 \times 10^3$ | $-24 \times 10^3$ |

### 3.1. Mixture SG EOS

With the help of the phases EOS, the mixture EOS is readily obtained. The mixture specific internal energy definition reads:

$$\rho e = \sum_k \alpha_k \rho_k e_k$$

By using SG EOS (15), each product $\rho_k e_k$ can be written as:

$$\forall k, \quad \rho_k e_k = \frac{p_k + \gamma_k p_{\infty,k}}{\gamma_k - 1} + \rho_k q_k$$

Under pressure equilibrium, we obtain the closure relation for Systems (2) and (14):

$$p(\rho, e, \alpha_k, Y_k) = \frac{\rho\left(e - \sum_k Y_k q_k\right) - \sum_k \frac{\alpha_k \gamma_k p_{\infty,k}}{\gamma_k - 1}}{\sum_k \frac{\alpha_k}{\gamma_k - 1}} \tag{19}$$

With this mixture EOS, the diffuse interface models derived previously reproduce propagation of acoustic disturbance at the Wood speed of sound (Wood, 1930):

$$\frac{1}{\rho c_w^2} = \sum_k \frac{\alpha_k}{\rho_k c_k^2} \tag{20}$$

This sound speed has a non-monotonic behavior versus volume fraction, as shown in Fig. 4. Systems (2) and (14) are strictly hyperbolic with the characteristic waves speeds: $u + c_w, u - c_w$ and $u$. When stiff heat and mass transfer effects are involved in System (14), the sound speed decreases to the thermodynamic equilibrium one, that still has a non-monotonic behavior versus volume fraction, but that is lower than the mechanical equilibrium (20) speed of sound. In this limit, the flow model (14) also reduces to the mixture Euler equations with equal pressures, equal temperatures and equal Gibbs free energies as closure relations. The details regarding this limit situation and reduced model are given in Saurel et al. (2008).

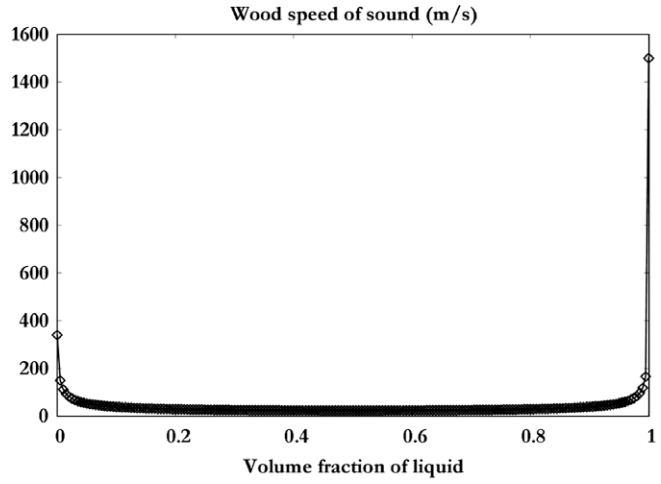


**Fig. 4.** Wood's speed of sound versus liquid volume fraction for a liquid–vapor water mixture.

## 4. Numerical results and validations

The numerical method to solve the compressible multi-phase flow model of diffuse interfaces (14) with heat and mass transfer proceeds in two steps. At each time step, the hyperbolic system in absence of heat and mass transfer is solved. This provides the hydrodynamic solution. Then stiff thermal and chemical relaxations are solved at liquid–vapor interfaces only. The interfaces are detected from the knowledge of volume fraction fields. The hydrodynamic solver is fully detailed in Saurel et al. (2009) and its extension to an arbitrary number of phases is used here. This solver is not conventional as the hyperbolic system is not conservative. The stiff differential solver for heat and mass transfer is specifically derived in Saurel et al. (2008). The model capabilities are illustrated in this section on various test problems involving interfaces of simple contact as well as evaporating interfaces. When available, comparisons are done with exact solutions or experimental ones.

One-dimensional tests are first performed for flows with interfaces in shock tubes, with or without evaporation fronts. Second, two-dimensional configurations are considered. The flow around a non-deformable high-velocity projectile impacting onto a liquid tank is computed and is quantitatively compared to experimental data. The last simulation deals with the simulation of the flow around and in the wake of an underwater missile.

### 4.1. Liquid–air shock tube

In this example, the left part of a shock tube is filled with liquid water at high pressure $p_l = 10^9$ Pa with density $\rho_l = 1000$ kg/m$^3$. The right chamber is set at atmospheric pressure and filled with air at density $\rho_v = 1$ kg/m$^3$. The initial discontinuity is located at $x = 0.75$ m in a 1-m length tube. For numerical reasons, each chamber of the tube contains a weak volume fraction of the other fluid (typically $10^{-8}$). SG EOS parameters are given in Table 1 concerning liquid water. Air is treated as an ideal gas with specific heat ratio $\gamma_{air} = 1.4$. In the first example, the liquid–gas interface is solved as a simple contact discontinuity: heat and mass transfer are not considered. The results are shown at time $t = 271$ μs in Fig. 5 and consist of three conventional waves. From left to right, a left-facing rarefaction wave propagating through the liquid, a right-facing contact discontinuity, moving from left to right and a right-facing shock propagating through the air. The numerical

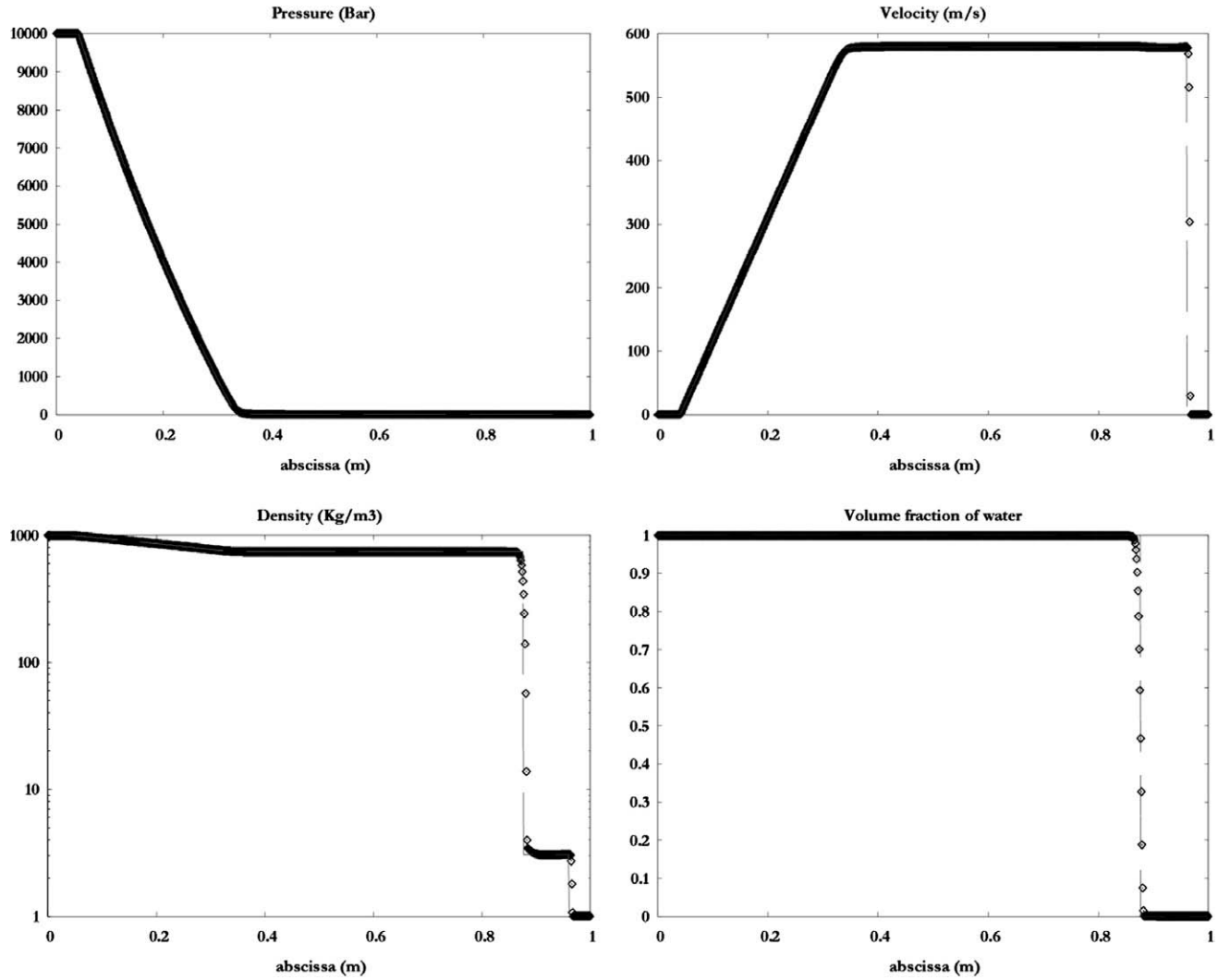


**Fig. 5.** Shock tube with non-miscible fluids. The numerical solution (symbols) is compared to the exact one (lines). The mesh involves 800 cells. Excellent agreement is observed and the solution is oscillation free even with very large initial density and pressure ratios.

solution is compared to the exact one and shows a perfect agreement. This test clearly shows that the method is able to deal with material interfaces governed by different EOS, and is accurate with the various continuous and discontinuous waves even with very large density and pressure ratios.

### 4.2. Evaporation front propagation in a shock tube

We now consider heat and mass transfer to simulate evaporation front propagation in a shock tube filled with dodecane. In this example, the left part of a shock tube is filled with liquid dodecane at high pressure $p_l = 10^8$ Pa with density $\rho_l = 500$ kg/m$^3$. The right chamber is set to atmospheric pressure and filled with vapor dodecane at density $\rho_v = 2$ kg/m$^3$. SG EOS parameters for liquid and steam dodecane are referred in Table 2. The initial discontinuity is located at $x = 0.75$ m in a 1-m length tube. For numerical reasons, each chamber of the tube contains a weak volume fraction of the other fluid (typically $10^{-8}$). The rarefaction wave propagation transforms the stable high pressure liquid dodecane to a superheated liquid and evaporation has to be considered at the interface (Fig. 6). An additional left-facing wave (evaporation front) appears between the rarefaction wave and the contact discontinuity. It propagates through the superheated liquid and produces a liquid–vapor mixture at thermodynamic equilibrium and high velocity. This evaporation front is also associated to a large pressure decrease. Experiments in shock tube have been carried out in (Simoes-Moreira and Shepherd, 1999) and confronted to numerical results in Saurel et al. (2008) showing very good agreement.

### 4.3. High velocity projectile impact onto a liquid tank

A high velocity spherical projectile is fired with a velocity of 1270 m/s onto a liquid tank. The projectile is made of tungsten alloy (DENAL) which density is 16 690 kg/m$^3$. The liquid container is made of PMMA with 20 mm thickness, transparent for visualizations, and filled with liquid water. A grid is stuck on the PMMA container. As it is placed between the light spots and the camera, shock propagation in the liquid is made visible as it modifies liquid optical properties. Grid deformations are recorded with the high speed camera. With the help of the high illumination device the cavitation pocket that appears in the wake is also visible. A schematic representation of the experimental facility and a typical experimental result are presented in Fig. 7. From the experiments qualitative and quantitative observations are obtained. The measured impact velocity is 1243 m/s, the projectile crossing time in the tank is 820 μs and the residual velocity is 569 m/s when the

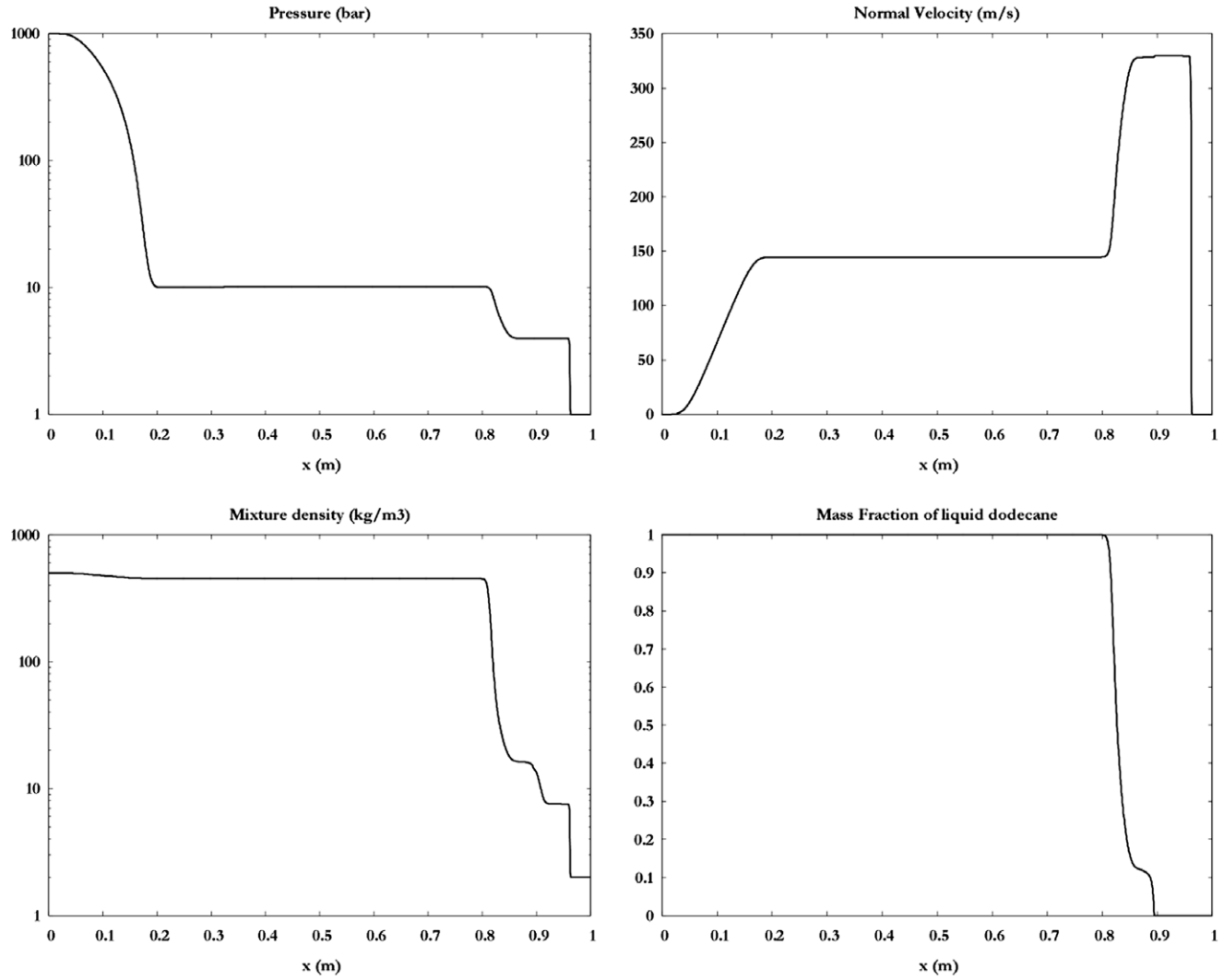


**Fig. 6.** Dodecane liquid–vapor shock tube with mass transfer. The thermo-chemical solver is used at the interface. An extra wave appears producing evaporation of superheated liquid. The second jump in mass fraction corresponds to the contact discontinuity separating the liquid–vapor mixture produced by evaporation and shocked vapor initially present in the right chamber. The velocity graph shows fluid acceleration through the evaporation front.

projectile exits the tank. Each photograph from experiments allows determination of the projectile location, the size of the cavitation wake and shock wave location in liquid water (Fig. 7, right side). Another important information is given by the projectile recovery at the end of the experiment: its spherical form is preserved almost perfectly, so that it is legitimate to neglect its deformation (Lecysyn et al., 2008). Consequently the flow model (14) is used with 4 fluids to model this system: liquid water, vapor water, air and solid projectile. In order to deal with the non-deformable projectile, a correction is done to the computational cells belonging to the projectile. Their velocity is reset to those of the projectile center of mass and the same correction is done regarding the kinetic energy in the total energy definition, at constant local total energy. The center of mass velocity is obtained by integrating over the entire domain the projectile momentum divided by the corresponding mass:

$$\vec{u}_{cm} = \frac{\int_\Omega \alpha_s \rho_s \vec{u}}{\int_\Omega \alpha_s \rho_s}$$

Corresponding computational results are shown in Fig. 8 at time $t = 0.133$ ms. The DENAL projectile is located closed to the tank center. A mixture of liquid water and steam is ejected from the impact location. The shock wave position in water and the cavitation wake are clearly visible. We now consider quantitative validation of the model against experiments. From the experiment it is possible to record the projectile trajectory versus time, as shown in Fig. 9. This characteristic trajectory can be fitted by an analytical relation based on a simplified formulation of the projectile momentum equation with constant drag coefficient:

$$\rho V \frac{\partial u}{\partial t} = -\frac{1}{2} C_d \rho_l A u^2 \tag{21}$$

where $\rho_l$ and $\rho$ represent, respectively, water and projectile densities, $V$ is the projectile volume, $A$ represents its frontal section ($A = \pi r^2$) where $r$ is the projectile radius and $C_d$ (dimensionless) the drag coefficient. With constant drag coefficient, solutions of (21) agree with less than 5% error with experiments. Direct integration of Eq. (21) results in projectile velocity and location determination. By denoting $m = \rho V$ the mass of the projectile, $u_0$ the impact velocity, $x = x_0 = 0$ the initial impact position at time $t = t_0 = 0$, we obtain for the velocity:

$$u(t) = \frac{u_0}{1 + \frac{C_d \rho_l A u_0}{2m} t}$$

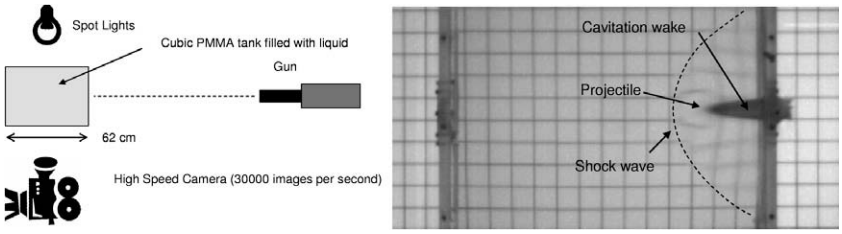


**Fig. 7.** High velocity spherical projectile fired onto a liquid tank. On the left, the experimental facility is schematically represented. On the right, a typical experimental result is reported showing the shock wave position and the cavitation wake.

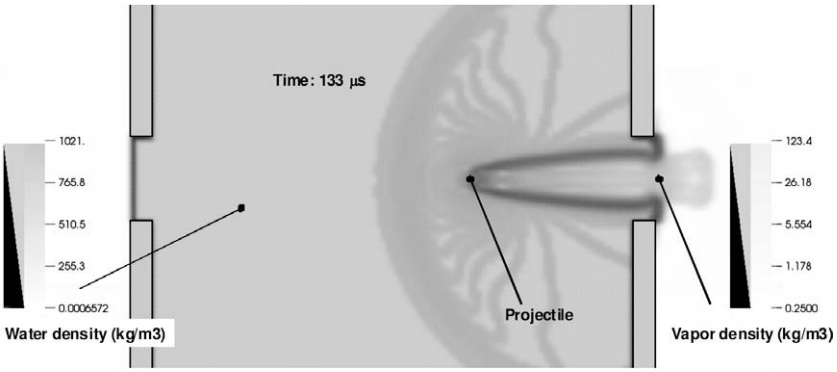


**Fig. 8.** High velocity spherical projectile fired onto a liquid tank. Density contours are plotted at time $t = 0.133$ ms showing the shock wave position as well as the cavitation wake and the projectile location.

And for the trajectory:

$$x(t) = \frac{2m}{C_d \rho_l A} ln\left(1 + \frac{C_d \rho_l A u_0}{2m} t\right) \tag{22}$$

Obviously, $C_d$ is a parameter, determined from the experimental trajectory. In Fig. 9, cross symbols represent the values recorded from the experiments, circle symbols represent the analytical curve from Eq. (22) with $C_d = 0.41$. The black squares are computational results from System (14) resolution. Excellent agreement is reported at any time. The same agreement is obtained for the projectile velocity versus time, as shown in Fig. 10. In addition, the total crossing time of the projectile is very well reproduced. The recorded travel time is 820 µs in the experiments and 815 µs in the computations. The computed exit residual velocity is 530 m/s to be compared to the experimental one of 569 m/s.

Last, we compare computational and experimental results in the entire domain at various times. The photographs from the experiments are shown on top of Fig. 11 at times $t = 133$ µs on the left and $t = 300$ µs on the right. Shock wave location can be determined from the grid stuck onto the tank, that is distorted during shock propagation. The cavitation wake is clearly visible in dark area. In the same figure but in lower part, we have superimposed

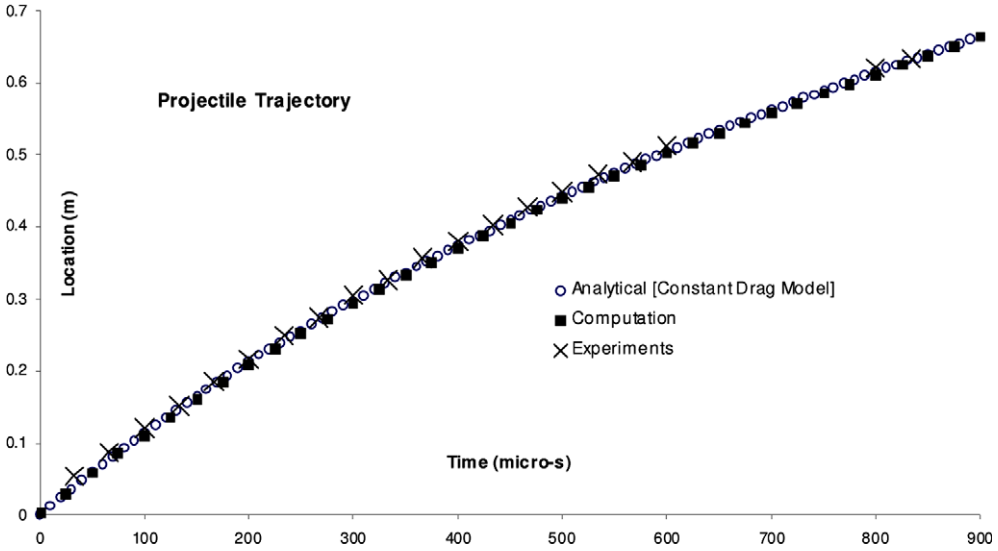


**Fig. 9.** Projectile trajectory versus time. Experimental results are represented by cross symbols, circles symbols correspond to the analytical solution with constant drag coefficient and black squares symbols represent computational results. Excellent agreement is observed at any time.

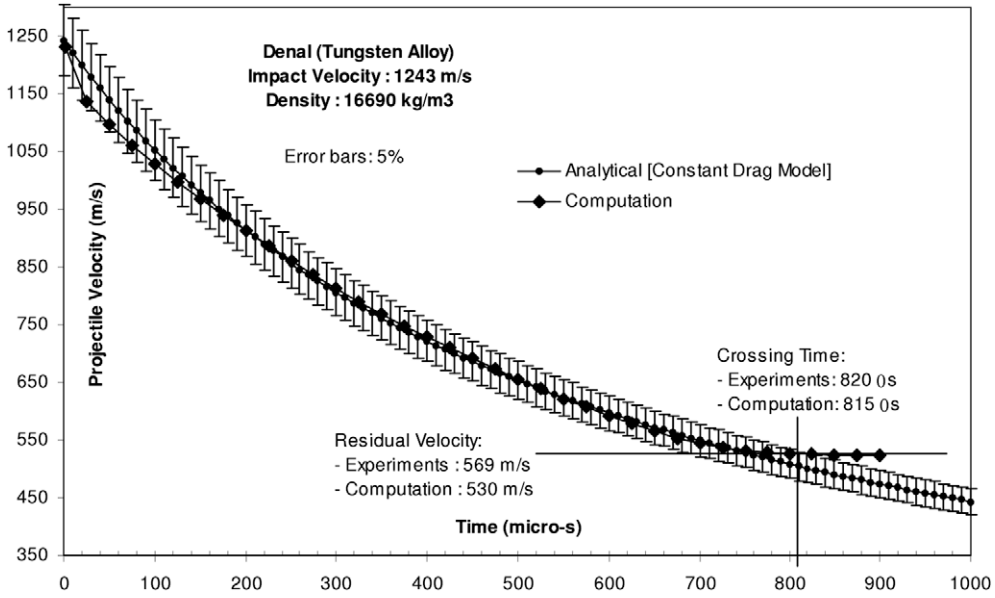


**Fig. 10.** Projectile velocity versus time. The analytical constant drag model solution is shown with dash–dot lines. An error bar with 5% error around the analytical solution is shown. Computational results are shown with black squares symbols. They always stay inside the error bar of 5%).

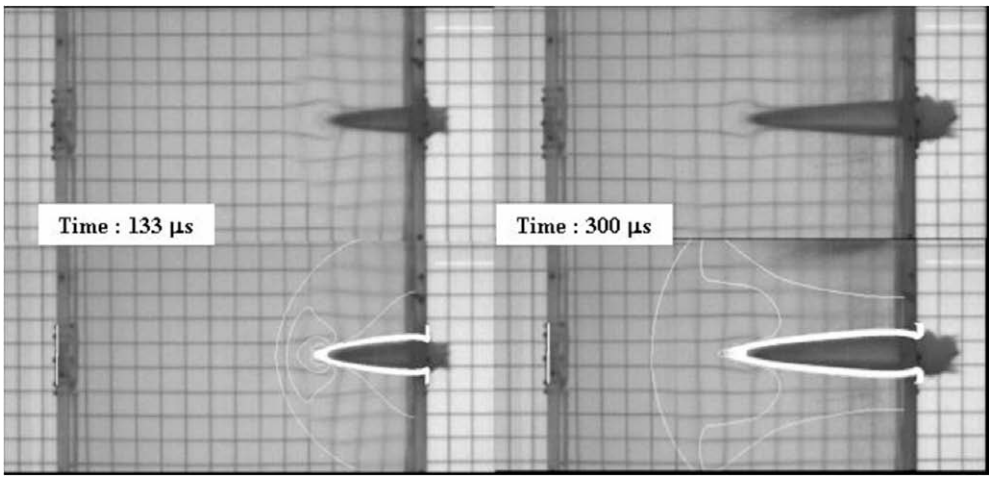


**Fig. 11.** High velocity spherical projectile fired onto a liquid tank. Computational results (density contours) are superimposed with experimental photographs at time $t = 0.133$ ms on the left and time $t = 0.3$ ms on the right.

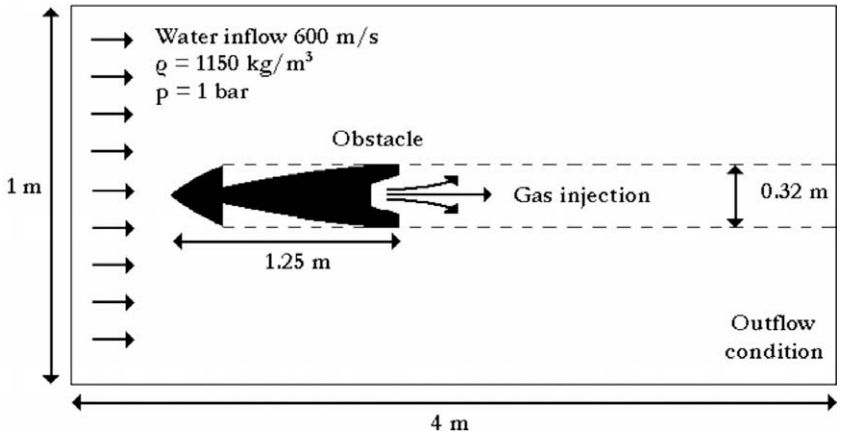


**Fig. 12.** Initial configuration for the underwater solid rocket motor computation.

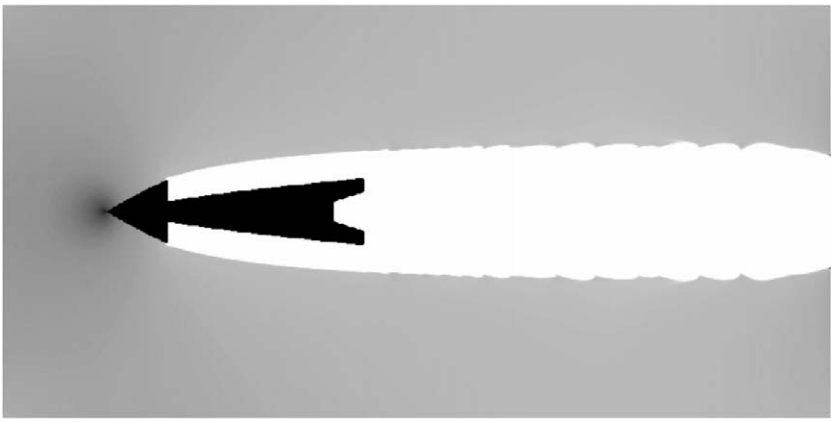

**Fig. 13.** Rocket motor moving at high velocity underwater. Mixture density contours are shown. The cavitation pocket composed of propulsion gases and steam is clearly visible.

computed liquid water density contour. The shape, size and location of the cavitation pocket is in perfect agreement. The location of the shock wave is clearly recovered too. The ejected mixture from the orifice also shows excellent agreement too.

### 4.4. Underwater missile

The last test illustrates model's capabilities to treat interfaces with and without phase transition. The typical situation under interest consists in an underwater missile moving at very high velocity. In the present simulation the solid rocket motor is represented by an immersed obstacle surrounded by liquid water at velocity 600 m/s. Liquid water is initially at atmospheric pressure with a density of 1050 kg/m$^3$. A weak volume fraction of vapor ($\alpha_v = 10^{-3}$) is initially present into the liquid. A non-condensable gas is ejected through the rocket nozzle. In Fig. 13, compression waves at the rocket's head are visible and the pressure exceeds 2000 atm. Then the flow undergoes strong rarefaction waves at geometrical singularities and the pressure decreases below the saturation pressure resulting in liquid evaporation. Combustion gases ejected through the nozzle fill the major part of the pocket. An aspiration phenomenon is also visible in Fig. 14 where the propulsion gas moves upstream in the rocket's head direction.

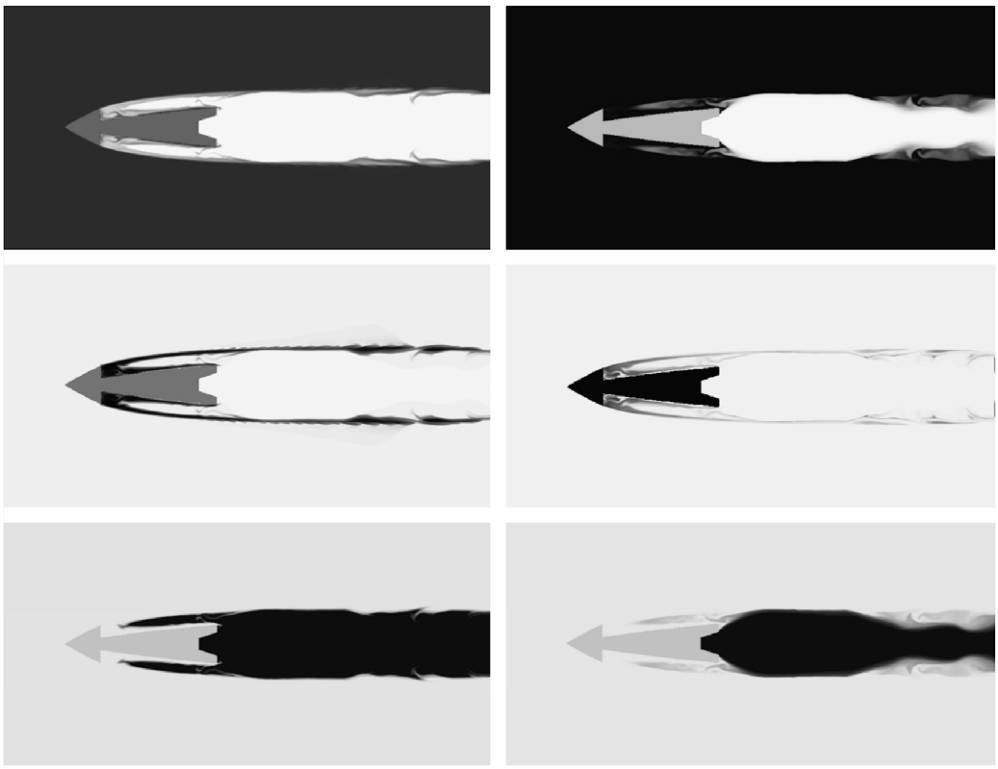

**Fig. 14.** Rocket motor moving at high velocity underwater. The left column corresponds to volume fraction contours, while, the right one corresponds to mass fraction contours. From top to bottom, these two variables are shown for liquid, vapor and inert gas, respectively. The black color is used in the regions where the considered fluid is present. The gas ejected from the rocket nozzle fills the major part of the cavitation pocket. Nevertheless, at the pocket boundary a small mass fraction of vapor (less than 0.1) is present. A portion of combustion gas products move upstream, in the rocket's head direction.

## 5. Conclusions

A relatively simple compared to the problem complexity and efficient formulation has been built in order to deal with interfaces, metastable liquids, cavitating flows and shocks in several space dimensions. The simplicity is due to a flow model valid at each point location, whose resolution is possible with a single numerical strategy. Examples with interfaces of simple contact and evaporating fronts are shown and validated against exact solutions and experimental data.

In the future it is planned to investigate capillary effects coupling (Perigaud and Saurel, 2005) in this diffuse interface theory to deal with the direct numerical simulation of evaporating and flashing bubbles and drops.

## References

Baer, M., Nunziato, J., 1986. A two-phase mixture theory for the deflagration-to-detonation transition (DDT) in reactive granular materials. Int. J. Multiphase Flows 12, 861–889.

Chinnayya, A., Daniel, E., Saurel, R., 2004. Computation of detonation waves in heterogeneous energetic materials. J. Comput. Phys. 196, 490–538.

Kapila, A., Menikoff, R., Bdzil, J., Son, S., Stewart, D., 2001. Two-phase modeling of DDT in granular materials: reduced equations. Phys. Fluids 13, 3002–3024.

Le Metayer, O., Massoni, J., Saurel, R., 2004. Elaborating equations of state of a liquid and its vapor for two-phase flow models. Int. J. Therm. Sci. 43, 265–276.

Lecysyn, N., Dandrieux, A., Heymes, F., Slangen, P., Munier, L., Lapebie, E., Le Gallic, C., Dusserre, G., 2008. Preliminary study of ballistic impact on an industrial tank: projectile velocity decay. J. Loss Prevent. Process Indust. 21, 627–634.

Liu, T., Khoo, B., Xie, W., 2004. Isentropic one-fluid modelling of unsteady cavitating flow. J. Comput. Phys. 201, 80–108.

Menikoff, R., Plohr, B., 1989. The Riemann problem for fluid flow of real materials. Rev. Mod. Phys. 61, 75–130.

Murrone, A., Guillard, H., 2005. A five equations reduced model for compressible two-phase flow problems. J. Comput. Phys. 202, 664–698.

Perigaud, G., Saurel, R., 2005. A compressible flow model with capillary effects. J. Comput. Phys. 209, 139–178.

Petitpas, F., Franquet, E., Saurel, R., Le Metayer, O., 2007. A relaxation-projection method for compressible flows. Part 2: artificial heat exchange for multiphase shocks. J. Comput. Phys. 225, 2214–2248.

Saurel, R., Abgrall, R., 1999. A multiphase Godunov method for compressible multifluid and multiphase flows. J. Comput. Phys. 150, 425–467.

Saurel, R., Gavrilyuk, S., Renaud, F., 2003. A multiphase model with internal degrees of freedom: application to shock–bubble interaction. J. Fluid Mech. 495, 283–321.

Saurel, R., Petitpas, F., Abgrall, R., 2008. Modelling phase transition in metastable liquids: application to cavitating and flashing flows. J. Fluid Mech. 607, 313–350.

Saurel, R., Petitpas, F., Berry, R., 2009. Simple and efficient relaxation methods for interfaces separating compressible fluids, cavitating flows and shocks in multiphase mixtures. J. Comput. Phys. 228, 1678–1712.

Simoes-Moreira, J., Shepherd, J., 1999. Evaporation waves in superheated dodecane. J. Fluid Mech. 382, 63–86.

Wood, A., 1930. A Textbook of Sound. G. Bell and Sons Ltd., London.